APPLIED PHYSICS LETTERS **109**, 143904 (2016)

Investigation of the behaviour of electronic resistive switching memory based on $MoSe_2$-doped ultralong Se microwires

Guangdong Zhou,[1] Bai Sun,[1,2] Yanqing Yao,[1] Huihui Zhang,[1] Ankun Zhou,[3,4] Kamal Alameh,[5] Baofu Ding,[1,5] and Qunliang Song[1,5,6,a)]

[1]*Institute for Clean Energy and Advanced Materials (ICEAM), Southwest University, Chongqing 400715, China*
[2]*Department of Physics, The University of Hong Kong, Pokfulam Road, Hong Kong 999077, China*
[3]*Kunming Institute of Botany, Chinese Academy Science, Kunming 650201, China*
[4]*Department of Chemistry, Tsinghua University, Beijing 100084, China*
[5]*Electron Science Research Institute, Edith Cowan University, 270 Joondalup Drive, Joondalup, WA 6027, Australia*
[6]*Chongqing Key Laboratory for Advanced Materials and Technologies of Clean Energy, Chongqing 400715, China*

(Received 23 May 2016; accepted 30 August 2016; published online 6 October 2016)

$MoSe_2$-doped ultralong Se microwires of length/diameter ratio in the order of $\sim$240 are synthesized by hydrothermal method. An electronic resistive switching memory (ERSM) device using a single $MoSe_2$-doped ultralong Se microwire is attained. The ERSM exhibits stable resistance ratio of $\sim 10^2$ for 5000 s, highly stable performance during 500 stressing cycles, and excellent immunity to the frequency of the driving voltage. By investigating the dynamic processes of trap filling, de-trapping, and free-charge migration, trap-controlled space-charge-limited current mechanism is found to dominate the observed ERSM behaviour. *Published by AIP Publishing.*
[http://dx.doi.org/10.1063/1.4962655]

Nowadays, non-volatile flash memory based products, such as digital cameras, laptops, MP4 players, and mobile phones, have attracted great attention over the last decades.[1,2] According to the prediction from the international technology roadmap for semiconductors (ITRS, 2013),[3] semiconductor manufacturing will enter an age of 5 nm technology in the year 2020. Following the conventional Si technology-based non-volatile flash memory advantages, an electronic device with ultrahigh storage density, low power consumption, and prolong retention time is urgently demanded in the near future. Numerous research and development activities are now focused on the development of the flash memory materials as well as structures to meet this demand. In particular, resistive random access memory (RRAM) has received special attention and been regarded as one of the most promising candidates of next generation non-volatile flash memory devices, due to its many advantages such as simple sample fabrication, low power consumption, fast writing/erasing speed of $\sim$ns, and prolonged retention time of >10 years.[4] The RRAM behaviour has been observed in many employing oxide films,[5–17] 2-dimension materials,[18–20] nanowires,[21,22] and even organic semiconductors.[23–25] The electronic resistive switching memory (ERSM) behaviour, which is the characteristic of asymmetric current-voltage (I–V) shapes as one important kind of RRAM, has been observed in many materials such as ZnO nanowires, MoO_3 nanobelts, $BiFeO_3$ nano-islands, and eumelanin nanofilms.[26–29] Different mechanisms have been reported on the explanation of the ERSM behaviour, of which the trap-controlled space-charge-limited current (SCLC) is widely adopted.[30–32] Other mechanisms including (1) the migration of ionic defects, such as the oxygen vacancies, for RRAM based on the oxide materials, resulting in the modulation of the effective thickness of the highly conductive oxide layer that contains the oxygen vacancies;[33–35] (2) the formation of metal ionic conducting filaments (because of the diffusion and rupture of metal ions injected from the electrodes) for organic-material-based RRAM;[36–38] and (3) the electrochemical metallization process for composite-oxide-based RRAM, whereby the metal ions are dissolved in redox reactions from electrochemically active electrodes.[39,40] It is important to note that some ultra-thin-film- or ultra-short-wire- based devices were found to exhibit ERSM behaviour, and although several above mechanisms including SCLC have been used to explain their ERSM behaviour, it is still not clear which mechanism is the dominant one.[30,32,33,41] Specifically, for the micrometer-scale film or the wire based RRAM, the relative large-scale physical dimension significantly decreases the migration of metallic ions or oxygen vacancies between electrodes,[42] which is quite common in a nanometer-scale RRAM. Therefore, developing micrometer-scale ERSM device will possibly provide a way to figure out the dominant mechanism, because the influence of migration process can be suppressed in the micrometer-scale RRAM devices.

In this letter, $MoSe_2$-doped ultralong Se microwires are synthesized and the ERSM behaviour of this single microwire is systematically investigated at room temperature. Experimental and fitting results indicate that the Mo^{4+}-induced trap-controlled SCLC mechanism dominates the ERSM behaviour. The ERSM device with the symmetry structure of Ag/$MoSe_2$-doped-Se/Ag was prepared at room temperature, and the doped Se microwires were synthesized by hydrothermal method. First, 0.1 mol $(NH_4)_6Mo_7O_{24}\cdot 4H_2O$

[a)]Author to whom correspondence should be addressed. Electronic addresses: qlsong@swu.edu.cn and qunliang@gmail.com

and 0.1 mol Se powder were mixed and dissolved in 50 ml deionized water at room temperature, labelled as Solution I. Second, another solution (solution II) was prepared by adding 0.05 g hexadecyl trimethyl ammonium bromide into the prepared solution I, followed by continuous stirring of solution II for 3 h. Third, solution II was transferred into a Teflon-lined steel autoclave, and heated at 500 K for 48 h. The ultralong $MoSe_2$-doped-Se microwires were consequently obtained from the hydrothermal treating solution II. Finally, the single doped Se microwire was horizontally placed between the two pre-deposited $50\,\mu m \times 50\,\mu m$ Au electrodes on the SiO_2/Si substrate, and then the Ag paste was dropped on both ends of the microwire.

Figure 1(a) shows a scanning electron microscopy (SEM, FE1450) image of the single $MoSe_2$-doped Se microwire. As shown in Fig. 1(a), the length and diameter of the nanowire are $\sim 600\,\mu m$ and $\sim 2.5\,\mu m$, respectively, resulting in a length/diameter ratio of ~ 240. The energy dispersive analysis (EDX) was used to characterize the chemical elements of the fabricated microwires, as displayed in Fig. 1(b). It is obvious that only two peaks with energies of 1.4 keV and 2.3 keV were detected, which correspond to Se and Mo elements, respectively. Therefore, the microwires only contain Se and Mo elements. A further estimation based on the peak intensities gives weight percentages of Mo (3.81%) and Se (96.19%), as shown in the inset of Fig. 1(b), and hence, the mole ratio of $MoSe_2$ in the $MoSe_2$-doped Se microwires is 3.5%. Note that microwires with other mole doping ratios were also developed by varying the mole ratio between $(NH_4)_6Mo_7O_{24}{\cdot}4H_2O$ and Se; however, only low-quality fragments or much shorter microwires could be synthesized. Therefore, the 3.5% mole doping ratio of $MoSe_2$ was the optimum value that realizes the longest uniform $MoSe_2$-doped Se microwires.

The chemical components of the $MoSe_2$-doped-Se microwires were further confirmed using X-ray photoelectron spectroscopy (XPS, 250Xi). The XPS spectrum in our equipment was calibrated by using the C 1s line of adventitious hydrocarbon on the specimen surface, which has a binding energy of 284.8 eV. Two peaks with binding energies of 232.28 eV and 235.54 eV were observed, as shown in Fig. 1(c). These peaks correspond to Mo $3d_{5/2}$ and Mo $3d_{3/2}$, respectively, which originate from the Mo-Se bond. Figure 1(d) shows the XPS spectrum for the Se 3d state. The typical peaks for Se^{2-} and Se^0 in the 3d state are at binding energies of 54.72 eV and 55.52 eV, respectively, which are contributed by the composite Mo-Se bond and the element Se, respectively.[43,44]

Therefore, the XPS results in conjunction with the EDX results, shown in Figs. 1(c) and 1(d), reveal that the synthesized microwire is composed of pure Se and $MoSe_2$. Generally, the charge storage capability of the ERSM is mainly dependent on the number of traps.[30] Therefore, in this work, the traps were deliberately introduced by doping $MoSe_2$ into the Se microwires with a mole ratio of 3.5%.

Figure 2(a) shows the I–V curve of the developed $MoSe_2$-doped-Se microwire, exhibiting a typical ERSM behaviour. For the first scan stage 1, the device is in the OFF state, namely, the high resistance state (HRS). With a forward bias voltage between 0 and 1.5 V, a negligible current is generated. As the applied voltage increases over 1.5 V, the current value sharply increases and the value reaches a maximum value at 3 V. This corresponds to the "SET" process when the device operates as a ERSM. By sweeping the applied voltage in the reversed direction ($3 \rightarrow 0$ V), the scan stage 2, the device switches to the ON state, namely, the low resistance state (LRS). Similarly, the scan stages 3 ($0 \rightarrow -3$ V) and 4 ($-3 \rightarrow 0$ V) correspond to LRS and HRS, respectively. The interface of Ag/Se can partially contribute to the observed ERSM behavior.[27,29,30,45] Taking into account the Mo^{4+} traps at the interface and in the microwire, there are two possible reasons for this asymmetric behaviour, either an asymmetric barrier or/and asymmetric distribution of traps is generated at the initial sweeping.

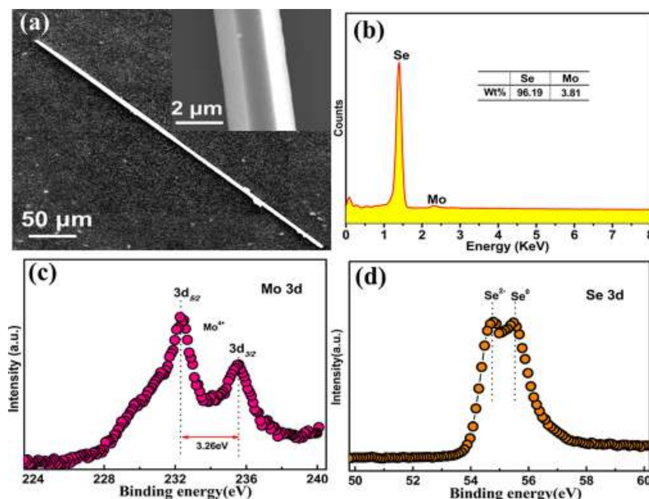

FIG. 1. (a) SEM images of the developed $MoSe_2$-doped-Se microwire; an enlarged image is shown in the inset. (b) EDX spectrum of $MoSe_2$-doped-Se microwires, which implies that the Se microwires is doped by 3.5% $MoSe_2$. XPS spectrum for (c) the Mo 3d and (d) Se 3d states, respectively, showing the intensity of the binding energy peaks of the $MoSe_2$-doped-Se microwire.

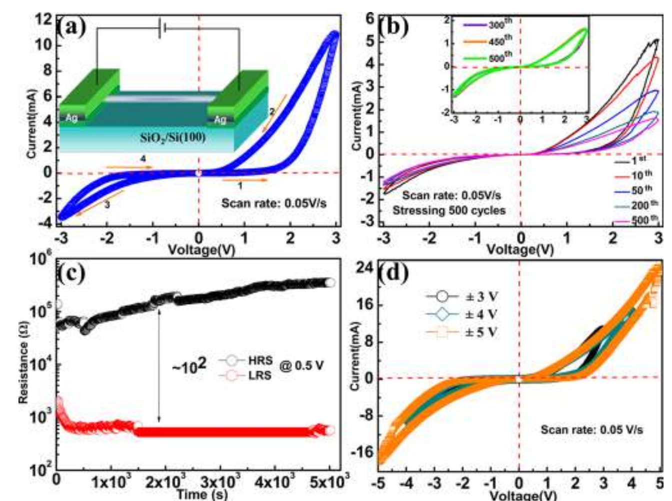

FIG. 2. (a) Measured voltage sweep plot for the developed $MoSe_2$-doped-Se microwire device. Voltage scan rate is 0.05 V/s. Asymmetric resistance switching behaviour is displayed. The inset shows the schematic diagram of device structure. (b) The retention property of the fabricated devices after 500 cycles. The inset is the 300th, 450th, and 500th cycle curve. (c) The resistance of the $MoSe_2$-doped-Se microwire in HRS and LRS at 0.5 V reading voltage. (d) Endurance characteristics for different voltage levels and a voltage scan rate of 0.05 V/s.

To investigate the retention stability and cycling endurance of the developed device, the bias voltages were swept between −3 V and 3 V for 500 cycles at a voltage scan rate of 0.05 V/s. Figure 2(b) shows the I–V curves for the 1st, 10th, 50th, 200th, and 500th cycles, respectively. It is obvious from Fig. 2(b) that for all 500 cycles the asymmetrical shape of the hysteresis I–V curves are well maintained, despite the fast drop of current in the first 50 cycles. After that, the device enters a slow-decaying stage until the 300th cycle, where the ERSM becomes stable as evidenced by the I–V curves shown in the inset of Fig. 2(b). Since the trap states dominate the ERSM behaviour, which will be discussed later, this decay and retention can be easily understood and explained as follows. The decay contains three regimes: sharp decay region (1st–50th), slow decay region (50th–300th), and stable region (300th–500th). In the initial stage, electrons are easily captured by shallow trap sites, and also easily released from these shallow trap sites. As a result, the current exhibits a large value. As the increase of cycling, the deep traps may be filled; some of the injected electrons might be captured by these deep traps, which is difficult to be released until a high bias voltage is applied. In addition, the electrons in the deep traps can function as the scattering centres to scatter the injected electrons. Therefore, from 1st to 300th cycle, the I–V shape shows an obvious decay. After stressing for 300 cycles, no more deep traps were filled. The electrons "programming" and "erasing" reach a relative saturation. Therefore, from 300th to 500th cyclings, the I–V shape shows an excellent stability.[27,30,45] Therefore, from 1st to 300th cycle, the I–V shape shows an obvious decay. After stressing for 300th cycles, nearly all of the deep traps arouse, and the electrons "programming" and "erasing" reach a relative saturation. Therefore, after operating sweep voltage from 300th to 500th, the I–V shape shows an excellent stability. This demonstrates the excellent endurance of the developed ERSM.

The retention time of the fabricated device was also investigated. Figure 2(c) shows the resistance of the developed device for the HRS and LRS versus time, revealing a stable resistance ratio of $\sim 10^2$ at a reading voltage of 0.5 V at room temperature even after continuously operating the device for 5×10^3 s. In a typical retention test, the HRS generally shows degradation over time because the trap-sites will be gradually filled. However, the retention test of Fig. 2(c) shows an opposite behavior, namely, HRS becomes higher while LRS becomes lower over time, indicating the existence of an additional effect. In this experiment, the retention test is carried out in the ambient environment at room temperature. The direct exposure to the air allows the absorption of moisture by the doped microwires or the Ag electrodes. In this case, the rupture of the formed bond and change of hydroxyl will possibly happen due to the coexistence of moisture and an external DC field (0.5 V reading voltage). An additional barrier is consequently generated, and results in the increased HRS.[46,47] The impact of the voltage range on the behaviour of the device was also investigated, to better understand its endurance characteristics at room temperature, as shown in Fig. 2(d). One can see that the asymmetrical I–V curves is well maintained even for the voltage range [−5 V, 5 V].

The ERSM behaviour and asymmetric shape of the I–V curve at the scan rate 20 V/s is shown in Fig. 3(a). The curve

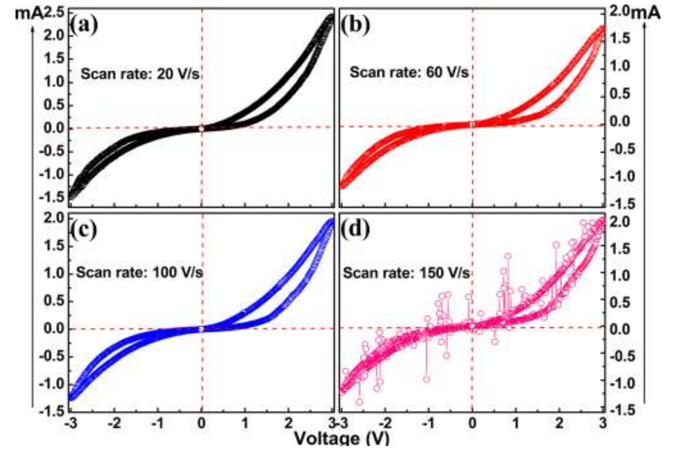

FIG. 3. I–V curves of the developed $MoSe_2$-doped-Se microwire ERSM device with for scan rates (a) 20 V/s; (b) 60 V/s; (c) 100 V/s; and (d) 150 V/s, respectively. The operating voltage range was (−3 V, 3 V).

is almost the same as that for the scan rate 0.05 V/s shown in the inset of Fig. 2(b). For the scan rates between 60 V/s and 100 V/s, slight changes are observed in relation to the asymmetric shape and the maximum current, as shown in Figs. 3(b) and 3(c). When the scan rate increases to 150 V/s, the ERSM behaviour can be maintained, despite it is unstable and noisy, as shown in Fig. 3(d).

To verify which mechanism dominates the ERSM behaviour of the single $MoSe_2$-doped-Se microwire based device, the HRS and LRS in the forward I–V curves for the 1st and 500th cycles are plotted separately at a scanning rate of 0.05 V/s, with logarithm scales used for the voltage and current coordinates. Figure 4(a) shows the I–V curve in the HRS for 1st cycle, which is comprised of four regions, namely, (i) the ohmic-like low conduction part (0–0.4 V), (ii) $I \sim V^2$ governed region (0.5–0.7 V), (iii) $I \sim V^4$ governed region (0.7–1.5 V), and (iv) $I \sim V^5$ governed region (1.5–3 V). The I–V curve in the HRS for the 500th cycle is shown in Fig. 4(b), which reveals (1) the ohmic-like low conduction region (0–0.15 V), (2) $I \sim V^2$ governed region (0.2 → 1 V), and (3) $I \sim V^4$ governed region (1–3 V). Figures 4(c) and 4(d) show the I–V curves in LRS for 1st cycle and 500st cycle, respectively, which consists of (1) ohmic-like low conduction region (0 → 0.1 V) and (0 → 0.03 V) for the 1st cycle and 500th cycle, respectively, and (2) $I \sim V^2$ governed region (0.1 → 3 V) and (0.03 → 3 V) for the 1st cycle and 500th cycle, respectively. According to the SCLC model, the current density can be described as follows:[30,41]

$$J \propto \frac{V^{m+1}}{L^{2m+1}}, \tag{1}$$

where V is the applied external voltage, L is the length of single $MoSe_2$-doped-Se microwire, m is the fitting index ($m \geq 0$). For m = 0, J is proportional to V, demonstrating the ohmic-like characteristics as shown in the inset of Fig. 4(a) and Figs. 4(a)–4(d). Note that a non-zero current at 0 V is observed, which results from the slow discharge of the reserved charges in the bulk or interfaces of the device. In this case, free electrons mainly come from thermally activated electrons in the bulk of microwires, while the electrons injected from the electrodes are negligible since the applied

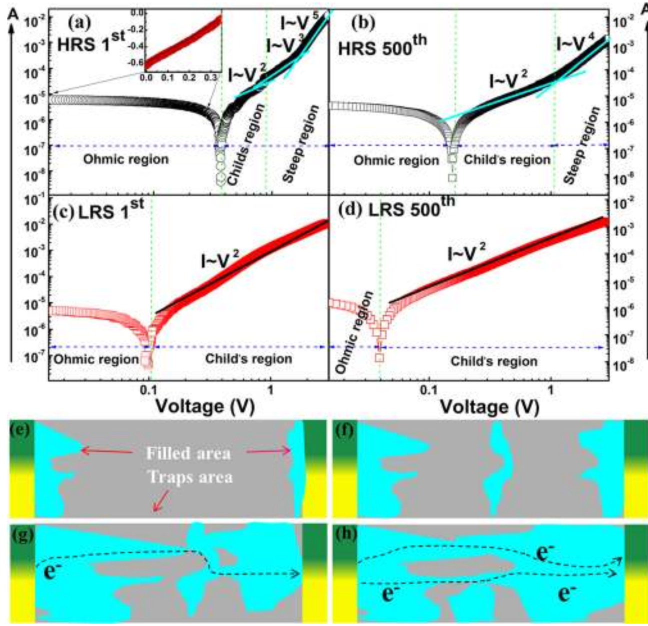

FIG. 4. Double logarithmic I–V curves and corresponding fitting results. The fitting results of LRS for 1st (a) and 500th (b), and HRS for 1st (c) and 500th (d), respectively. Schematic graphs of the SCLC mechanism containing the pristine states (e), traps-filling process (f), establishing the conductive paths (g), and freely migration of charges region (h), respectively.

voltage is low. Therefore, the current is governed by the ohmic emission mechanism.

Figures 4(e)–4(h) schematically show the dynamic processes of (1) the initial stage, (2) trap-filling, (3) building of conductive paths, and (4) migration of free charges in the ERSM device. Here, the gray and light green regions represent the regions of empty traps and filled traps, respectively. As it is schematically shown, a portion of the injected electrons from the Ag electrode fill in the trap states as space charges, while the other injected electrons contribute to free electrons. Therefore, the current becomes trap-controlled space-charge-limited current. Generally, the SCLC can be described by Child's square law, namely, m = 1 in Eq. (1), and $I \propto V^2$, which can be expressed as follows:[25,30,41]

$$J = \left(\frac{\gamma}{\gamma + 1}\right) kV^2, \tag{2}$$

$$k = \frac{9\varepsilon_r \varepsilon_0 \mu}{8L^3}, \tag{3}$$

where J is the current density, γ is the ratio of free electrons/trapped electrons, ε_r is the relative permittivity, ε_0 is the vacuum permittivity, V is the applied voltage, μ is the carrier mobility, and L is the microwire length. In this work, k is maintained as a constant in the small voltage range of 0–3 V due to the fixed $\varepsilon_0\varepsilon_r$ and L values for a given microwire as well as the negligible change of μ in such small voltage range. Initially, when most of the electron trap states are vacant, γ is much smaller than 1 ($\gamma \ll 1$). Therefore, Eq. (2) can be rewritten as $J = \gamma kV^2$. Therefore, the small γ value determines the low current density at a given voltage, corresponding to the HRS. When the applied voltage increases beyond a given value, all of the trap states are occupied by the injected electrons, and the device is in ON state, namely, changing from HRS to LRS. At this state, the areas of filled traps are connected together to form the conductive path, as schematically shown in Figs. 4(g) and 4(h). The impact of the trap states on the concentration of free charge is then almost negligible, resulting in a sharp increase of the current, leading to $I \propto V^{m+1}$ ($m > 1$) as shown in Figs. 4(a) and 4(b). When the voltage sweeping direction is reversed, namely, from 3 V to 0 V, in the beginning, all the Mo^{4+} trap states have been filled with the electrons as formerly done in the forward direction. Therefore, the device is still in the ON state. By further reducing the voltage, a small portion of the electrons trapped in Mo^{4+} states undergoes a de-trapping process, leaving the trap states vacant. Consequently, the current flow through the device is dominated by the trap controlled SCLC again. Therefore, $I \sim V^2$ is observed as shown in Figs. 4(c) and 4(d) as well. It is important to note that, although some trap states are unoccupied during the reversed voltage sweeping direction, most of the Mo^{4+} trap states are still filled with electrons. In this case, most of the injected charges become free charges, i.e., $\gamma \gg 1$. Hence, Eq. (2) can be simplified as $J = kV^2$. In comparison with that ($J = \gamma kV^2$, $\gamma \ll 1$) in a forward sweeping direction ($0 \rightarrow 3$ V), the trap controlled SCLC ($J = kV^2$) in a reversed voltage sweeping direction ($3 \rightarrow 0$ V) is much higher, indicating that the device is in the LRS and the ON states. Based on the above discussion, we conclude that the ESRM behaviour of the $MoSe_2$ doped Se microwires is due to electron trapping and de-trapping from Mo^{4+} trap states and the current-voltage characteristic is dominated by the electron-trap-controlled SCLC mechanism.

In summary, $MoSe_2$ doped ultralong Se microwires with a length/diameter ratio of ~240 have been developed using hydrothermal synthesis. An ERSM behaviour with a stable resistance ratio of ~10^2 for 5000 s, stable performance during 500 retention testing cycles, and strong immunity to the voltage scan rate has been experimentally observed in a single $MoSe_2$-doped ultralong Se microwire based memory device. After carefully considering the dynamic process of the traps filling, de-trapping, and free-charge migration, we confirmed that the trap-controlled SCLC dominates the observed ERSM behaviours. The work provides a revelation on the development of next-generation, high-performance, low-cost memory device based on the trap controlled SCLC governed micrometer-scale devices.

This work was supported by the National Natural Science Foundation of China (Grant No. 11274256) and Fundamental Research Funds for the Central Universities (XDJK2014A006).

[1]S. Seo, M. Lee, D. Seo, E. Jeoung, D.-S. Suh, I. Hwang, S. Kim, I. Byun, J.-S. Kim, J. S. Choi, and B. H. Park, Appl. Phys. Lett. **85**, 5655–5657 (2004).
[2]L.-W. Feng, C.-Y. Chang, T.-C. Chang, C.-H. Tu, P.-S. Wang, Y.-F. Chang, M.-C. Chen, and H.-C. Huang, Appl. Phys. Lett. **95**, 262110 (2009).
[3]L. Wilson, *International Technology Roadmap for Semiconductors* (*ITRS*) (Semiconductor Industry Association, 2013).
[4]J. J. Yang, M.-X. Zhang, J. P. Strachan, F. Miao, M. D. P. R. D. Kelley, G. M. Ribeiro, and R. S. Williams, Appl. Phys. Lett. **97**, 232102 (2010).
[5]D. C. Kim, S. Seo, S. E. Ahn, D.-S. Suh, M. J. Lee, B.-H. Park, I. K. Yoo, I. G. Baek, H.-J. Kim, E. K. Yim, J. E. Lee, S. O. Park, H. S. Kim, U.-In. Chung, J. T. Moon, and B. I. Ryu, Appl. Phys. Lett. **88**, 202102 (2006).
[6]C. B. Lee, B. S. Kang, A. Benayad, M. J. Lee, S.-E. Ahn, K. H. Kim, G. Stefanovich, Y. Park, and I. K. Yoo, Appl. Phys. Lett. **93**, 042115 (2008).

[7]W. Guan, M. Liu, S. Long, Q. Liu, and W. Wang, Appl. Phys. Lett. **93**, 223506 (2008).
[8]S.-Y. Wang, D.-Y. Lee, T.-Y. Tseng, and C.-Y. Lin, Appl. Phys. Lett. **95**, 112904 (2009).
[9]L. Goux, P. Czarnecki, Y. Y. Chen, L. Pantisano, X. Wang, R. Degraeve, B. Govoreanu, M. Jurczak, D. Wouters, and L. Altimime, Appl. Phys. Lett. **97**, 243509 (2010).
[10]S. Yu, X. Guan, and H.-S. P. Wong, Appl. Phys. Lett. **99**, 063507 (2011).
[11]S. Yu, Y. Y. Chen, X. Guan, H.-S. P. Wong, and J. A. Kittl, Appl. Phys. Lett. **100**, 043507 (2012).
[12]C.-Y. Huang, C.-Y. Huang, T.-L. Tsai, C.-A. Lin, and T.-Y. Tseng, Appl. Phys. Lett. **104**, 062901 (2014).
[13]Y. Wang, K. Chen, X. Qian, Z. Fang, W. Li, and J. Xu, Appl. Phys. Lett. **104**, 012112 (2014).
[14]H. Sasakura, Y. Nishi, and T. Kimoto, Appl. Phys. Lett. **107**, 233510 (2015).
[15]F. Zhou, Y.-F. Chang, B. Fowler, K. Byun, and J. C. Lee, Appl. Phys. Lett. **106**, 063508 (2015).
[16]Y. F. Chang, B. Fowler, F. Zhou, Y. C. Chen, and J. C. Lee, Appl. Phys. Lett. **108**, 033504 (2016).
[17]T. L. Tsai, H. Y. Chang, J. C. Lou, and T. Y. Tseng, Appl. Phys. Lett. **108**, 153505 (2016).
[18]V. K. Sangwan, D. Jariwala, I. S. Kim, K.-S. Chen, L. J. Lauhon, and M. C. Hersam, Nat. Nanotechnol. **10**, 403–406 (2015).
[19]S. Bertolazzi, D. Krasnozhon, and A. Kis, ACS Nano **7**, 3246–3252 (2013).
[20]G. Liu, X. Zhuang, Y. Chen, B. Zhang, J. Zhu, C.-X. Zhu, K.-G. Neoh, and E.-T. Kang, Appl. Phys. Lett. **95**, 253301 (2009).
[21]S. I. Kim, J. H. Lee, Y. W. Chang, S. S. Hwang, and K.-H. Yoo, Appl. Phys. Lett. **93**, 033503 (2008).
[22]E. D. Herderick, K. M. Reddy, R. N. Sample, T. I. Draskovic, and N. P. Padture, Appl. Phys. Lett. **95**, 203505 (2009).
[23]H. S. Majumdar, A. Bandyopadhyay, A. Bolognesi, and A. J. Pal, J. Appl. Phys. **91**, 2433–2437 (2002).
[24]L. Bozano, B. Kean, V. Deline, J. Salem, and J. Scott, Appl. Phys. Lett. **84**, 607 (2004).
[25]H. Wang, F. Meng, B. Zhu, W. R. Leow, Y. Liu, and X. Chen, Adv. Mater. **27**, 7670–7676 (2015).
[26]M. Ambrico, A. Cardone, T. Ligonzo, V. Augelli, P. F. Ambrico, S. Cicco, G. M. Farinola, M. Filannino, G. Perna, and V. Capozzi, Org. Electron. **11**, 1809–1814 (2010).
[27]J. Song, Y. Zhang, C. Xu, W. Wu, and Z. L. Wang, Nano Lett. **11**, 2829–2834 (2011).
[28]G. Zhou, W. Zhao, C. Xu, X. Ma, and A. K. Zhou, J. Alloys. Compd. **679**, 47–53 (2016).
[29]S. Hong, T. Choi, J. H. Jeon, Y. Kim, H. Lee, H.-Y. Joo, I. Hwang, J.-S. Kim, S.-O. Kang, S. V. Kalinin, and B. H. Park, Adv. Mater. **25**, 2339–2343 (2013).
[30]Q. Liu, W. Guan, S. Long, R. Jia, M. Liu, and J. Chen, Appl. Phys. Lett. **92**, 12117 (2008).
[31]X. L. Shao, L. W. Zhou, K. J. Yoon, H. Jiang, J. S. Zhao, K. L. Zhang, S. Yoo, and C. S. Hwang, Nanoscale. **7**, 11063–11074 (2015).
[32]A. Carbone, B. K. Kotowska, and D. Kotowski, Phys. Rev. Lett. **95**, 236601 (2005).
[33]J. J. Yang, M. D. Pickett, X. Li, D. A. Ohlberg, D. R. Stewart, and R. S. Williams, Nat. Nanotechnol. **3**, 429–433 (2008).
[34]D. Lee, D.-J. Seong, I. Jo, F. Xiang, R. Dong, S. Oh, and H. Hwang, Appl. Phys. Lett. **90**, 122104 (2007).
[35]G. Zhou, B. Wu, X. Liu, Z. L. Li, S. Zhang, A. Zhou, and X. Yang, J. Alloys Compd. **678**, 31–35 (2016).
[36]F. M. Simanjuntak, O. K. Prasad, D. Panda, and C-A. Lin, Appl. Phys. Lett. **108**, 183506 (2016).
[37]G.-S. Park, X.-S. Li, D.-C. Kim, R.-J. Jung, M.-J. Lee, and S. Seo, Appl. Phys. Lett. **91**, 222103 (2007).
[38]G. Zhou, B. Wu, Z. Li, Z. Xiao, S. Li, and P. Li, Curr. Appl. Phys. **15**, 279 (2015).
[39]Y.-F. Chang, L. Ji, Z.-J. Wu, F. Zhou, Y. Wang, F. Xue, B. Fowler, E. T. Yu, P. S. Ho, and J. C. Lee, Appl. Phys. Lett. **103**, 033521 (2013).
[40]A. Wedig, M. Luebben, D.-Y. Cho, M. Moors, K. Skaja, V. Rana, T. Hasegawa, K. K. Adepalli, B. Yildiz, R. Waser, and I. Valov, Nat. Nanotechnol. **11**, 67–74 (2016).
[41]B. Cho, J. M. Yun, S. Song, Y. Ji, D. Y. Kim, and T. Lee, Adv. Funct. Mater. **21**, 3976–3981 (2011).
[42]G. Zhou, B. Wu, X. Liu, P. Li, S. Zhang, B. Sun, and A. Zhou, Phys. Chem. Chem. Phys. **18**, 6509–6514 (2016).
[43]K. Aretouli, P. Tsipas, D. Tsoutsou, J. Marquez-Velasco, E. Xenogiannopoulou, S. Giamini, E. Vassalou, N. Kelaidis, and A. Dimoulas, Appl. Phys. Lett. **106**, 143105 (2015).
[44]Y. Jin, D. H. Keum, S. J. An, J. Kim, H. S. Lee, and Y. H. Lee, Adv. Mater. **27**, 5534–5540 (2015).
[45]S. Kim, Y. J. Hu, S. Y. Choi, and Y. K. Choi, Appl. Phys. Lett. **97**, 033508 (2010).
[46]C. S. Yang, D. S. Shang, Y. S. Chai, L. Q. Yan, B. G. Shen, and Y. Sun, Phys. Chem. Chem. Phys. **18**, 12466–12475 (2016).
[47]X. Yang, B. J. Choi, A. B. Chen, and I. W. Chen, ACS Nano **7**, 2302–2311 (2013).